Supplemental Document

Biomedical Optics EXPRESS

Increasing the field-of-view in oblique plane microscopy via optical tiling: supplement

BINGYING CHEN,[1] BO-JUI CHANG,[1] FELIX Y. ZHOU,[1] STEPHAN DAETWYLER,[1] ETAI SAPOZNIK,[1] BENJAMIN A NANES,[1,2] ISABELLA TERRAZAS,[3,4,5] GABRIEL M. GIHANA,[1] LIZBETH PEREZ CASTRO,[6] ISAAC S. CHAN,[3,5,7] MARALICE CONACCI-SORRELL,[6,8,9] KEVIN M. DEAN,[1] ALFRED MILLETT-SIKKING,[10] ANDREW G. YORK,[10] AND RETO FIOLKA[1,*]

[1] *Lyda Hill Department of Bioinformatics, UT Southwestern Medical Center, Dallas, Texas, USA*
[2] *Department of Dermatology, UT Southwestern Medical Center, Dallas, Texas, USA*
[3] *Department of Internal Medicine, Division of Hematology and Oncology, UT Southwestern Medical Center, Dallas, Texas, USA*
[4] *Department of Immunology, UT Southwestern Medical Center, Dallas, Texas, USA*
[5] *Simmons Comprehensive Cancer Center, UT Southwestern Medical Center, Dallas, Texas, USA*
[6] *Department of Cell Biology, UT Southwestern Medical Center, Dallas, Texas, USA*
[7] *Department of Molecular Biology, UT Southwestern Medical Center, Dallas, Texas, USA*
[8] *Harold C. Simmons Comprehensive Cancer Center, UT Southwestern Medical Center, Dallas, USA*
[9] *Hamon Center for Regenerative Science and Medicine, University of Texas Southwestern Medical Center, Dallas, Texas, USA*
[10] *Calico Life Sciences LLC, South San Francisco, CA, USA*
[*] *Reto.Fiolka@UTSouthwestern.edu*

Supplement DOI: https://doi.org/10.6084/m9.figshare.21070243

Parent Article DOI: https://doi.org/10.1364/BOE.467969

Increasing the Field-of-View in Oblique Plane Microscopy via optical tiling: supplemental document

This document provides details of the dual-axis scan unit and its alignment, the illumination module, the performance of the ASLM mode, a numerical Aperture estimate of the OPM system, the single-galvo shear unit, data analysis (includes deconvolution, general guidelines for stitching data, and the 3D segmentation and meshing of volumetric data), and sample preparation of Keratinocytes, Colon cancer cell spheroid and Natural killer cells.

1. Dual-axis scan unit

We used Zemax and geometrical optics to design, analyze and present the working principle of the dual-axis scan unit in this section. Fig. S1(a-c) shows the 3D layout of the Zemax simulation model with 9 configurations (shown in different colors), which correspond to the output optical scanning angle of 0° and ±5° in each direction and could support the FOV of 12.2 x 12.2 mm^2 after the scan lens for point scanning. Fig. S1(d) shows a rendering of the CAD model for the dual-axis scan unit.

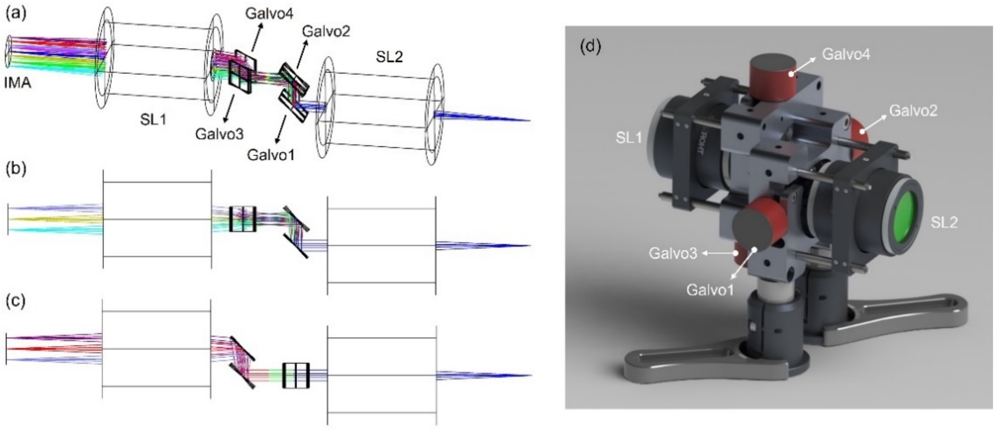

Fig. S1. (a-c) 3D Layout of the dual-axis scan unit and the adjacent scan lenses. SL1-2, Scan Lenses; IMA, image plane. Light is coming from the right. Tilted view (a), Side view (b), Top view (c). (d) CAD model of the mechanical assembly including the scan unit and the scan lenses.

Fig. S2(a) shows the spot diagram of 9 configurations at image plane [IMA, in Fig. S1(a)]. The black circle indicates the airy radius of around 8.37 µm and the RMS spot size in all configurations are well under the Airy radius. This simulation was done to illustrate the optical performance of the dual-axis scan unit. Its relevance to tiling OPM is as follows: It illustrates how an on-axis (central) image point is mapped to the center of each tile, and how it is being scanned to acquire a volume.

To compare the performance with a two-axis tip-tilt mirror (i.e. a mirror that can be tilted around two axes), we replaced the dual-axis scan unit with two mirrors overlapped at the focal plane of the scan lens in Zemax [shown in Fig. S2(b)]. The Huygens PSFs with the dual-axis scan unit and ideal two-galvo scan unit are shown in Fig. S2(c) and (d), respectively. The corresponding Strehl ratios are 0.766 and 0.765, which are similar and demonstrate that the distortion shown in the spot diagrams is from the chosen scan lenses, and not from the design of the dual-axis scan unit.

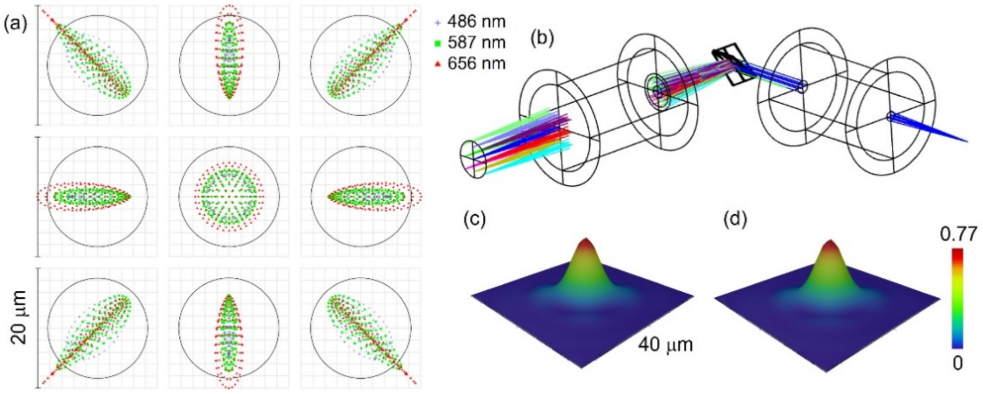

Fig. S2. (a) Configuration matrix spot diagram of the Zemax model for the dual-axis scanner. Here the chief ray is used as reference. Legend items refer to wavelength. (b) 3D Layout of the ideal two-galvo scanner with the same scan lenses. (c) Huygens PSF of the lower left configuration with the dual-axis scan unit. (d) Huygens PSF with the ideal two-axis scanner.

To compare the performance with a conventional two-axis scanning strategy, we replaced the dual-axis scan unit with two Galvos and a pair of relay lenses between them in Zemax [shown in Fig. S3(a)]. We used the Zemax model of the CLS-SL scan lens from Thorlabs for the relay lenses to minimize field dependent aberrations introduced by simpler lenses (e.g. achromatic doublet). Because only a “blackbox” Zemax model (which cannot be edited and can only be placed in certain ways) was available, we added a folding mirror after each Galvo, which is also a common way to place Galvos in the Y direction to maintain the lens train on the optical table. The matrix spot diagram shown in Fig. S3(b) indicated this scanning strategy suffers from larger field dependent aberrations (please note the different scaling). We tried to minimize the spot size (quick focus function in Zemax) by adjusting the distance between SL4 and the image plane (Fig. S3(c)). The theoretical distance is 53.931 mm, which increases to 54.050 mm after optimization.

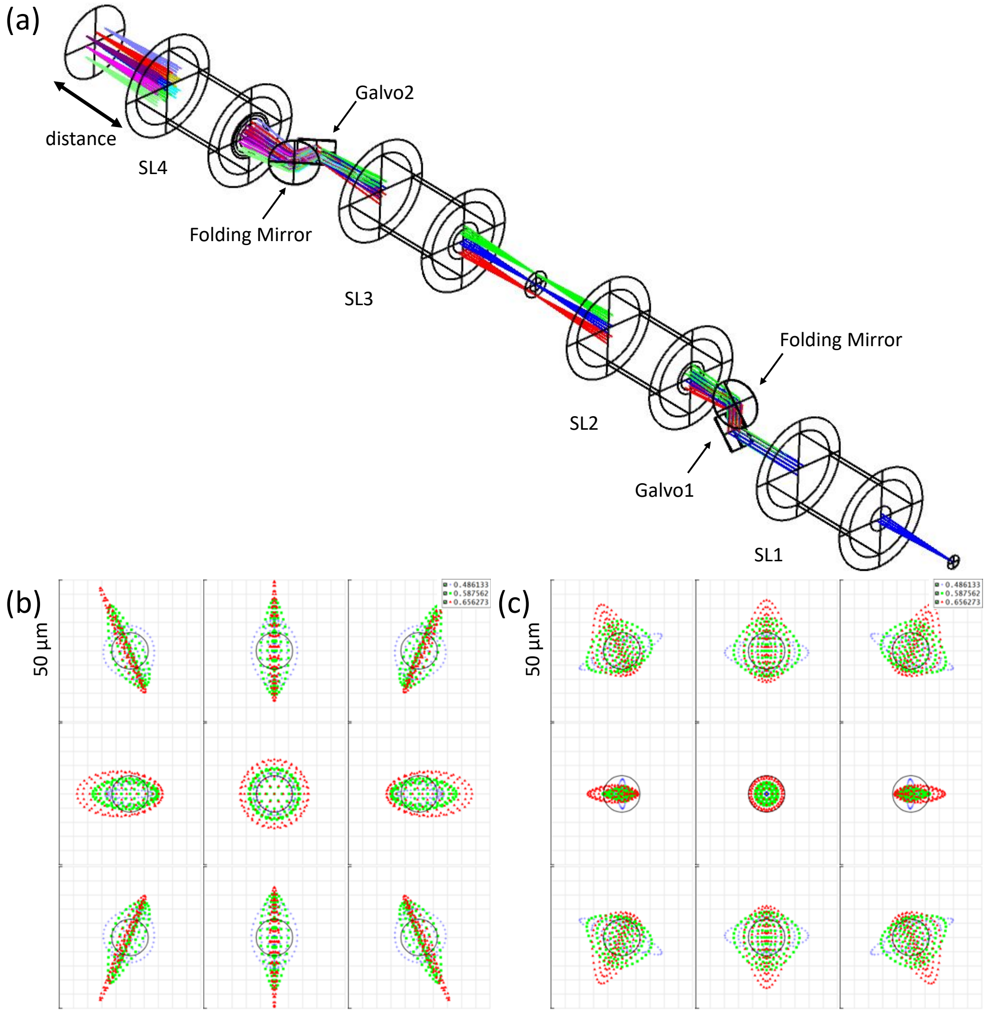

Fig. S3. (a) 3D Layout of the conventional two-galvo scanning system with the same scan lenses. (b. c) Configuration matrix spot diagram of the Zemax model for this system before (b) and after (c) focus optimization. Here the chief ray is used as reference. Legend items refer to wavelength.

Furthermore, we simulated how three points, at the center and the edges of a tile, are mapped by the dual-axis scanning unit to the extended field of view. We did this simulation both for the dual-axis scan unit [Fig. S4 (a)], and for the conventional two galvo system with a relay lens pair [Fig. S4 (b)]. While the central spot (center in blue box) appears similar in size for both systems, much wider spots are observed off-axis in Fig. S4 (b) for the conventional scan unit.

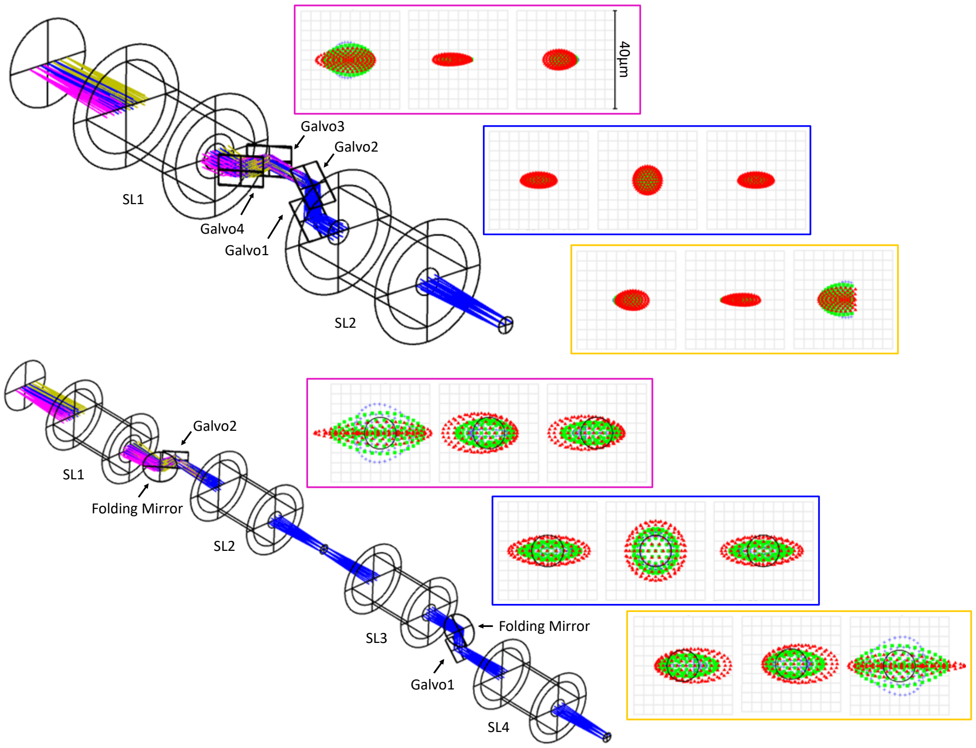

Fig. S4. Performance of the dual-axis and conventional scan unit in mapping three input spots to the three different tiles (shown as magenta, blue and yellow). (a) 3D Layout of the dual-axis scan unit and spot diagrams for the three tiles. (b) 3D Layout of the conventional two galvo scan unit with relay lenses, and the spot diagrams for the three tiles. All spots are plotted over a 40x40 µm wide grid.

The optical scanning angle of our dual-axis scan unit with the Thorlabs GVS211 galvanometric mirrors is limited to ±5°. The Zemax simulation illustrates ray clipping of the galvo at the extreme scan position, which causes the slight degradation of resolution in the x axis (Fig. 2(a)). As shown in Fig. S5(a) and Fig. S5(b), the three beams in different colors indicate three points (center and both ends) illuminated by the light sheet at the optical scanning angle of ±5° [see also green volumes in Fig. 1(g)]. The green light in Fig. S5(c) and the red light in Fig. S5(d) show ray clipping at both ends.

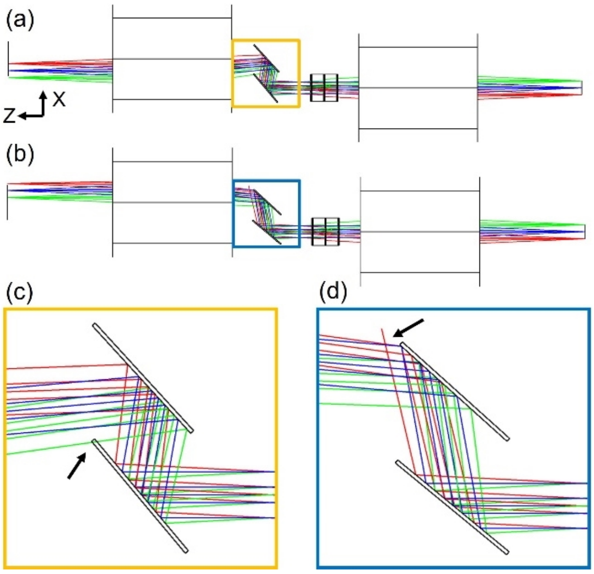

Fig. S5. (a) 3D Layout of the dual axis scan unit and the adjacent scan lenses in the light-sheet condition with the optical tiling angle of 5°. (b) 3D Layout with the optical tiling angle of -5°. (c, d) Zoom-in of the box in (a) and (b), respectively. Arrows indicate the ray clipping.

The ray clipping introduces some non-uniformity and vignetting over the FOV, as shown in Fig. S6. Of note, the beam clipping depends on the beam size in infinity space, thus on the size of Back Focal Plane (BFP) of the objective. The clipping could be alleviated by using objectives with smaller BFP size or using larger Galvo mirrors as Galvo 2 and 3 in the scan unit.

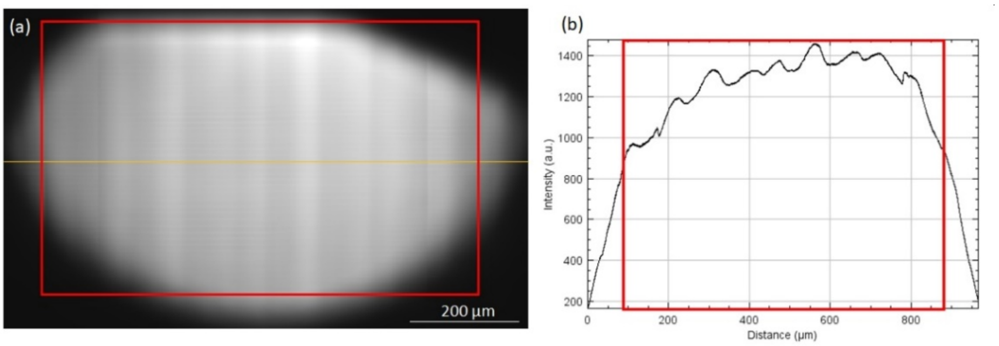

Fig. S6. (a) Image of water fluorescein mixture, acquired with optical tiling OPM. Red rectangle encompasses a field of view of 800 x 500 µm. (b) Intensity along the yellow line in (a). In Red is a bounding box for a range of 800 µm.

The Zemax simulation shows the feasibility of the dual-axis scan unit. We further use geometrical optics to demonstrate the relation between two Galvos and the common point in each Galvo pair. Fig. S7(a) and Fig. S7(b) show the working principle of Pair 1 and Pair 2, which correspond to Fig. 1(d) and Fig. 1(e).

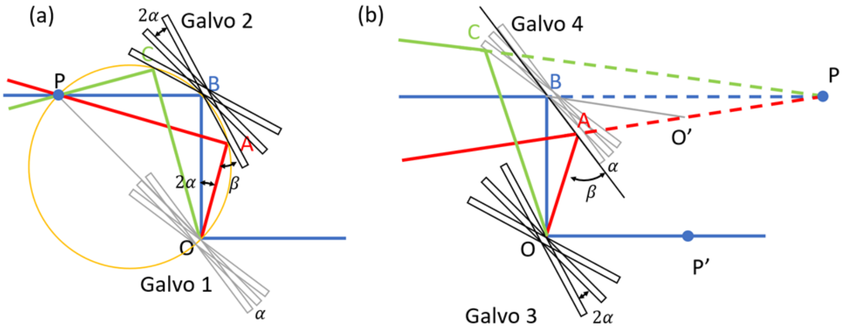

Fig. S7. Working principle of dual-axis scanner. (a) Galvo pair 1. (b) Galvo pair 2. P’ is the common point P in (a).

For Pair 1[shown in Fig.S7(a)], we first demonstrate that if the scanning angle of Galvo 2 is twice the scanning angle of Galvo 1, all laser beams will pass through a common point P. This can be proved by showing that points A, B, O, P are on one circle (P is the intersection point of laser beams with the scan angle of 0 and 2α). Then, we can show the distance between the common point P and Galvo 2 equals to the distance between the two Galvos, which means OB = BP.

If we rotate Galvo 1 for α to get the red beam, the optical scanning angle $\angle AOB$ will be 2α. If we then rotate Galvo 2 for 2α, we have

$$\angle ABO = 45^\circ - 2\alpha.$$

$$\because \beta = \angle ABO + \angle AOB = 45^\circ, \angle BAP = \beta,$$

$$\therefore \angle OAP = 90^\circ.$$

We already know $\angle OBP = 90^\circ$, then $\angle OAP = \angle OBP$. According to the inscribed angle theorem, we can demonstrate that A, B, O, P are on one circle.

Because points A, B, O, P are on one circle, we have

$$\angle APO = \angle ABO = 45^\circ - 2\alpha.$$

Then $\angle AOP = 90^\circ - \angle APO = 45^\circ + 2\alpha$, $\angle BOP = 45^\circ$. So ΔOBP is an isosceles right triangle and OB = BP.

Similarly, we can prove P is also the intersection point of laser beams with the scan angle of 0 and -2α (blue and green).

Therefore, all laser beams after Pair 1 will pass through the point P, and OB = BP.

Next, we can prove for Pair 2, when the scanning angle of Galvo 3 is set to twice the scanning angle of Galvo 4, a common virtual scan point P can be formed, as shown in Fig. S7(b).

If we rotate Galvo 3 for 2α to get the red beam, the optical scanning angle $\angle AOB$ will be 4α. Then if rotate Galvo 4 for α, we have

$$\angle ABO = 45^\circ - \alpha,$$

$$\angle BAO = 180^\circ - \angle ABO - \angle AOB = 135^\circ - 3\alpha.$$

$$\because \angle ABP = 45^\circ + \alpha, \angle BAP = \angle BAO = 135^\circ - 3\alpha,$$

$$\therefore \angle APB = 2\alpha.$$

We can add point O', which makes $AO' = AO$ and we can easily prove that $\Delta ABO'$ is congruent to ΔABO. Then we have $\angle AO'B = \angle AOB = 4\alpha$, $\angle O'BP = 90^\circ - 2(45^\circ - \alpha) = 2\alpha$, and consequently $\angle BPO' = 2\alpha$. Thus, $\Delta BO'P$ is an isosceles triangle, $O'B = O'P$, and

$$PB = 2 \cdot OB \cdot \cos(2\alpha).$$

According to the equation shown above, the distance between the virtual point P and Galvo 4 is irrelevant to the sign of α. Therefore, if Galvo 3 and 4 are rotated by -2α and $-\alpha$, respectively, shown as the green line in Fig. S7(b), the above equation stays valid. This conclusion can also be proved by similar geometric analysis. Besides, we can also notice that when α is a small angle, the distance between the virtual point P and Galvo 4 is two times the distance between the two Galvos, $PB \approx 2 \cdot OB$. But at a larger angle, PB is dependent to α, which means there is a little deviation of the position of the virtual point P. We derive the deviation as

$$\sigma PB = 2 \cdot OB \cdot [1 - \cos(2\alpha)].$$

In our case, $\sigma PB = 2 \times 15\ mm \times \left[1 - \cos(2 \times 5°)\right] = 0.456\ mm$. This will cause the primary optical axis to be slightly tilted away from the design oblique plane after the primary objective by $1.65°$ at the edge, which is neglectable in our application.

[Derivation of the primary optical axis angle: $\mathrm{atan}\left(\sigma PB \times \frac{\tan(2 \times 5°)}{f_{SL}}\right) \times M = 1.65°$, where f_{SL} and M are the focal length of scan lens and the magnification of the primary objective, $f_{SL} = 70\ mm$, $M = 25$.]

2. Alignment of the dual-axis scan unit

For the alignment of the dual-axis scan unit, the custom designed mount can be separated into two blocks, each of which holds one galvo mirror pair. To determine the right orientation of the galvo mirrors, small alignment holes are machined into each block. As shown in Fig. S8(a), an alignment laser (shown in red), travelling parallel to the optical table, must be deflected by the first galvo such that it passes through the alignment hole. Then the second galvo is inserted and rotated such that the alignment laser exits the unit parallel to the optical table, as shown in Fig. S8(b).

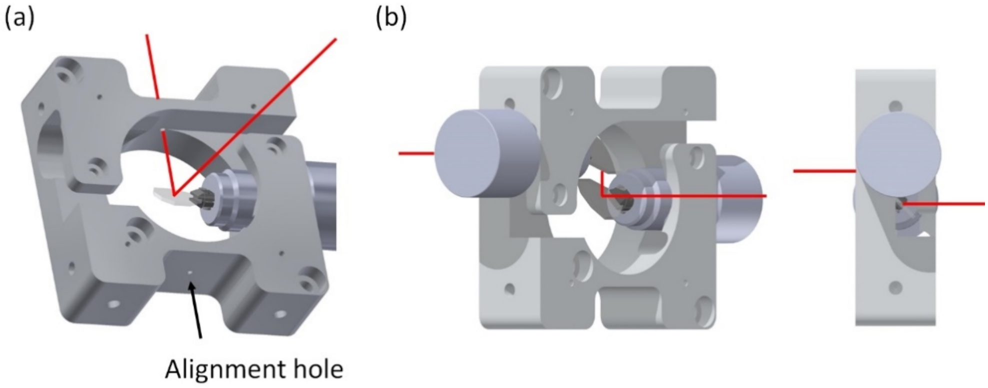

Fig. S8. Alignment of the galvo mirror in one of the two blocks of the dual-axis scanner. (a) An alignment laser (shown in red) travelling parallel to the optical table is reflected by the first galvo mirror such that it passes through the alignment hole. (b) The second galvo is aligned such that the laser exits the unit travelling again parallel to the optical table.

To adjust the correct drive amplitudes for the two galvo mirrors, a piece of paper is put on the side where the two galvo units would be joined, as shown in Fig. S9(a). The drive amplitudes can be varied relative to each other using a scaling amplifier. The correct setting is found when the common pivot point is on the plane of the paper sheet.

To position the scan lens, a collimated laser beam is sent into the unit. The Tube lens is translated until the focus lies on the plane where the two units will be joined. A sheet of paper or metal block can be used to visualize the laser focus, as shown in Fig. S9(b). The metal block will reflect laser speckles, which will become largest when the focus is incident on the metal surface [1]. Once both units are aligned this way, they can be joined together to form the dual-axis scan unit. At this stage, a collimated laser beam entering on one side should exit the unit again collimated, which verifies that the two scan lenses form a 4f system.

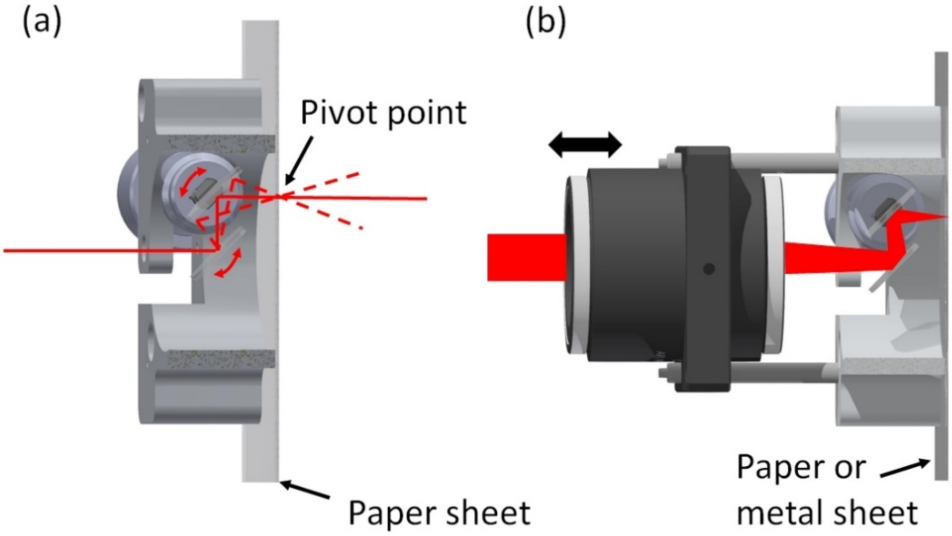

Fig. S9. Adjustment of the galvo drive voltages and the position of the scan lens. (a) A sheet of paper can be used to visualize the common pivot point. The drive voltages are correctly set if the pivot point coincides with the plane of the paper sheet. (b) The correct position of the scan lens can be found by focusing a collimated laser beam onto the sheet of paper. Alternatively, a metal sheet or block of metal can be used, which will reflect laser speckles. The laser speckles become largest if the laser is focused on the metal surface.

3. The illumination module

A schematic drawing of the illumination module is shown in Fig. S10(a). The output laser from a fiber coupled solid state laser module (OBIS Galaxy with laser modules LS 561nm-80mW, LX 488nm-100mW and LX 640nm-75mW, Coherent Inc) was first collimated by a fiber collimator (CFC11A-A, Thorlabs), then expanded in one dimension by a Powell lens and an achromatic lens L1 (2x AC254-030-A, Thorlabs) (shown in “side-view”). A telescope of achromatic doublets L2 (AC254-060-A, Thorlabs) and L3 (AC254-050-A, Thorlabs) images the light-sheet on a resonant galvo (CRS 4KHz, Cambridge technologies), which is conjugate to the image plane of the OPM system. This resonant galvo is used for shadow suppression by pivoting the light-sheet [2]. After the resonant scanner, an achromatic doublet L4 (AC254-040-A, Thorlabs) forms a 4F system with the tube lens TL2 [see also Fig. 1(a)] to conjugate the resonant scanner to the image plane of the OPM system. As shown in the top-view, an ETL (Electrically tunable lens, EL-16-40-TC, Optotune) is placed on the Fourier plane between L2 and L3 to refocus the waist of the light-sheet and the beam condition will be maintained in the other dimension. An adjustable slit is used to control the divergence of the light-sheet. The mirror after L4 is conjugate to the pupil plane of the primary objective. As such, changing the mirror tilt angle translates the light-sheet in the sample plane. We used a Gimbal Mirror Mount (U100-G2K, Newport) to ensure only the angle of the beam is tuned and no shift is introduced. We further replaced the manual adjustor of the mount with a piezo actuator (PIA25, Thorlabs) to allow motorized fine-tuning capability. The illumination unit sits on a large translation stage (#66-455, Edmund optics). When translating the whole illumination unit, the light-sheet incident angle can be varied in fine steps. Fig. S10(b) shows photo of the optical setup. The system is built to allow the ETL lying horizontally.

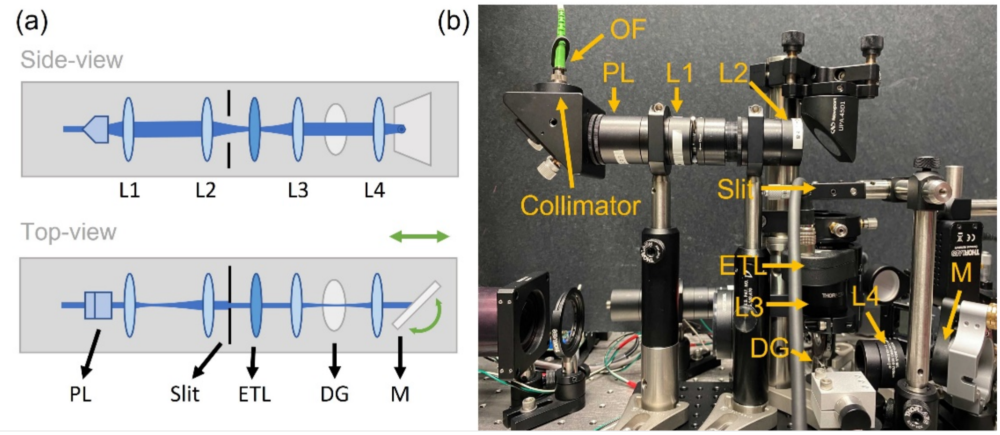

Fig. S10. (a) Schematic of the illumination unit in side-view and top-view. (b) Photo of the illumination unit. L1-4, Lenses; PL, Powell Lens; ETL, Electrically Tunable Lens; DG, Dither Galvo; M, Mirror; OF, Output fiber.

4. Axially Swept Light-Sheet Microscopy imaging mode

In standard light-sheet microscopy, a long and thick light-sheet is needed to cover a large sample, which results in a worse axial resolution. Axially Swept Light-Sheet Microscopy (ASLM) overcomes this challenge by axially sweeping a short, thin light-sheet and synchronizing the sweep of the light-sheet with the rolling shutter of the camera. With an ETL in our illumination unit, we can realize an ALSM imaging mode in OPM. We first used fluorescent nanospheres to measure the resolution [Fig. S11(a)]. For the thin light-sheet, the axial resolution (measured by the FWHM of the nanospheres in z) was around 1 µm at the waist of the light-sheet and increased to around 2 µm at the edge, while for the ASLM, an axial resolution of 1.01±0.14 µm was maintained throughout the volume. The axial resolution gain is modest, as the available NA for the light sheet is more limited than in a conventional ASLM system. However, the ASLM mode can help to homogenize axial resolution in an OPM system.

We further tested the performance of the ASLM in live sample by imaging the AKP (APC$^{-/-}$; KRAS$^{G12D/+}$; p53$^{-/-}$; TdTomato^{+}) organoids [3] in both modes [Fig. S11(b)]. The organoid cells are labelled by TdTomato and is visualized in magenta and Phalloidin is labelled by 488 AlexaFluor and shown in green.

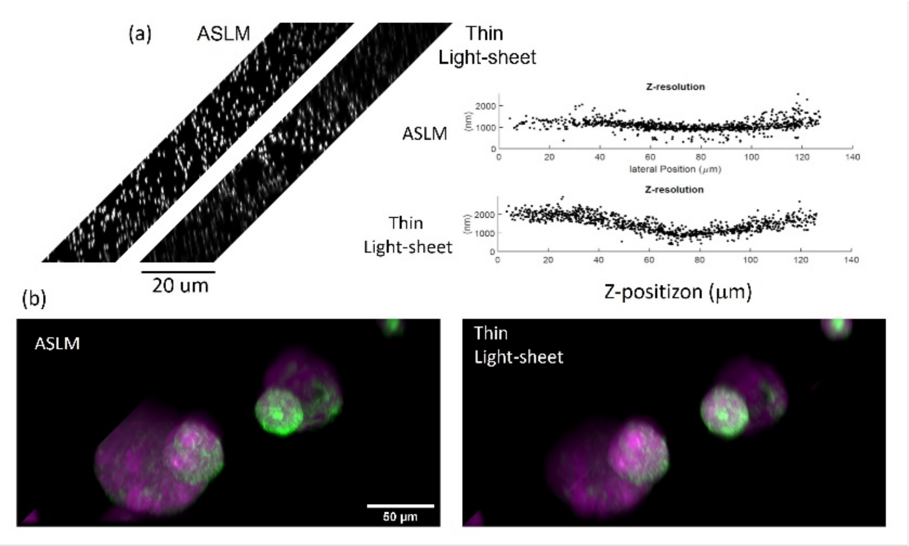

Fig. S11. (a) Fluorescent nanospheres (shown in y-z view) and their Full Width Half Maximum measurements in ALSM mode and thin light-sheet mode. (b) AKP Organoids imaged in ASLM mode and using a thin light-sheet.

5. Numerical Aperture estimate of the OPM system

OPM microscopes typically have an elliptically shaped effective pupil, and as such, there is no single value for the numerical aperture that would characterize the overall system. Nevertheless, one can define a lower bound numerical aperture for the direction where the light-collection is lowest. This is shown in Fig. S12.The half angle of the secondary objective is 53 degrees. In the tilt direction of the tertiary objective, some of the light cone coming out of the secondary is clipped to a maximum acceptance angle of 45 degrees. The half angle of the accepted cone becomes $(45^o+53^o)/2=49^o$, which corresponds to an numerical aperture of $n*\sin(49^o)=1$ for water immersion. The angular estimate ignores reflection losses at the glass surface of the tertiary objective. It is an estimate of the set of wavevectors that can be coupled in, but does not assign them a weight. In the orthogonal direction, the light cone coming from the secondary objective is not clipped, so the half angle of the accepted light-cone by the tertiary objective remains 53^o. This results in an NA of 1.06. The Primary objective supports an NA of 1.1.

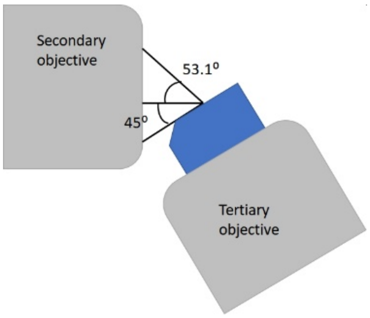

Fig. S12. Estimate of the light-cone that can be accepted by the tertiary objective.

6. Single-Galvo shear unit

Adding a pair of Galvo mirrors in front of the camera to shear the image has been demonstrated in [4] and is schematically shown in Fig. S13(a). Here we adopted a simpler implementation with a single-Galvo scanner as shown in Fig. S13(b) and demonstrate its virtually identical performance.

For both shear units, the optical path length will change for different shearing amounts, which in principle adds a small amount of defocus to the image. In addition, the single-Galvo shear unit adds a small amount of tilt of the image as it is being scanned, which compresses the images in the shear direction. These effects however turn out to be neglectable based on our analysis.

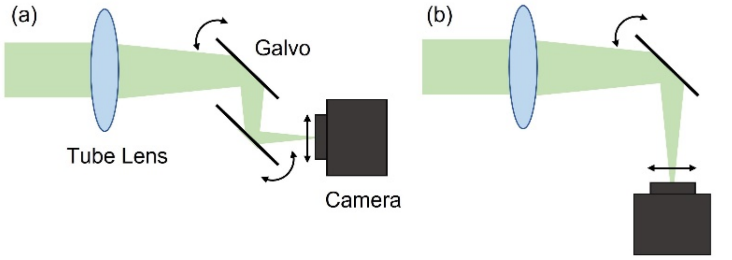

Fig. S13. Schematic of the shear unit with (a) dual-Galvo and (b) single Galvo.

To calculate the variation of the optical path length at the surface of the camera chip, we drew the optical axis of convergent fluorescence light without shearing (blue lines, shown in Fig. S14) and with the shear angle α (red lines). The shear angle will shift the optical axis by x at the surface of the camera chip (dashed lines). The length difference of the red lines and blue lines is the light path difference.

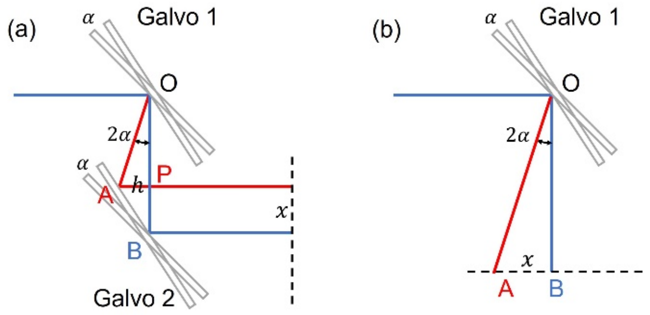

Fig. S14. Working principle of dual-Galvo shear unit (a) and single-Galvo shear unit (b).

For dual-Galvo shear unit as shown in Fig. S14(a), the light path difference is OA+AP-OB. When the Galvo rotated by α, the optical scanning angle is 2α, then we have $\angle AOB = 2\alpha$, $\angle ABO = 45° - \alpha$. Defining $OB = d$, $AP = h$, we have

$$h = OP \cdot \tan(2\alpha) = PB \cdot \tan(45° - \alpha),$$

$$OP + PB = OB,$$

$$\therefore OP + PB = \left(\frac{\tan(45° - \alpha)}{\tan(2\alpha)} + 1\right)x$$

$$= \frac{x}{\sin\,(2\alpha)} = d.$$

Therefore, the light path difference for dual-Galvo unit is

$$OA + AP - OB$$

$$= \frac{h}{\sin(2\alpha)} + h - d = x\tan(45° - \alpha)\left(\frac{1}{\sin(2\alpha)} + 1\right) - d\ = -2\sin^2(\alpha)d = -2d\sin^2\left(\frac{1}{2}\,\mathrm{asin}\left(\frac{x}{d}\right)\right).$$

For single-Galvo shear unit, the light path difference is

$$OA - OB = \sqrt{x^2 + d^2} - d.$$

Therefore, we can get the focal plane deviation with the camera chip as abscissa under different conditions, shown in Fig. S14(a). For the dimensions chosen in our setup, *i.e.* the galvo is placed 110 mm in front of the camera in the single-Galvo shear unit (OB in Fig. S14(b)), and the distance between two galvos in the dual-Galvo shear unit is 25.4 mm (OB in Fig. S14(a)), the maximum focal plane deviation is around 0.2 mm for single-Galvo shear unit and -0.88 mm for dual-Galvo shear unit. For -0.88 mm deviation, the corresponding focal shift in sample space is 0.23 μm, which is still below the depth of focus of the OPM imaging system. Nevertheless, if we extend the distance between the galvos in the dual-Galvo shear unit, we can see the deviation is close to the single-Galvo shear unit (orange line in Fig. S15(a)). Given the large distance from the single-Galvo shear unit to the camera chip, the tilted optical axis will lead to a 99.8% compression of the images at the extremes of the scan range. The compression is the ratio of the projection of the tilted image to the un-tilted image, which is a simple cosine relation and is cos(3.46°) in this case. The focal plane with equal light path length (blue lines) at different shear angle is shown in Fig. S15(b) and (c).

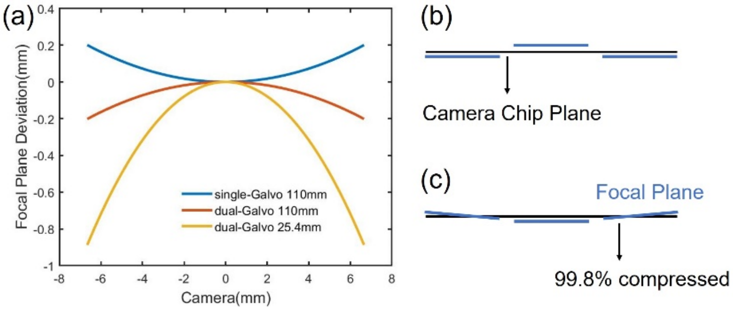

Fig. S15. (a) Focal plane deviation at camera chip. Schematic of focal plane deviation for (b) dual-Galvo unit, and (c) single-Galvo unit.

7. Deconvolution and resolution analysis

To evaluate the resolution in a live cell imaging context, we preformed image decorrelation analysis [5] on ARPE cells labeled with EGFP for AP2 before [Fig. S16(a)] and after [Fig. S16(b)] deconvolution. Before the deconvolution, we up-sampled the image by a factor of 2 through zero padding at the Fourier Transform image. Using image decorrelation analysis on the whole image, the lateral resolution is 408 nm [Fig. S16(c)] in the raw data, and 294 nm [Fig. S16(d)] after deconvolution.

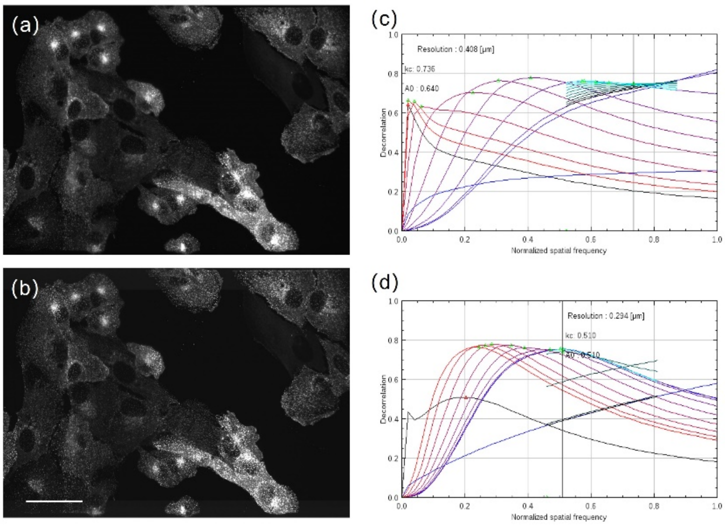

Fig. S16. (a) Maximum projection of parental human retinal pigmented epithelium (ARPE-19) cells with EGFP-labeled AP2. (b) After up-sampling and deconvolution. (c) Decorrelation analysis of a plane of (a). (d) Decorrelation analysis of the same plane in (b).

To evaluate the resolution in a live cell imaging context and across the FOV after tiling, we preformed image decorrelation analysis [5] on human keratinocyte cells expressing mNeonGreen tagged keratin 5 before [Fig. S17(a-c)] and after [Fig. S17(d-f)] deconvolution. Before the deconvolution, we up-sampled the image by a factor of 2 through zero padding at the Fourier Transform image. Fig. S17 (b, c, e, f) show two examples of the effect after deconvolution. Such examples can be seen across the whole FOV if we zoom in to different regions in Fig. S17 (a, d). Using image decorrelation analysis on the whole image, the lateral resolution is 444 nm [Fig. S17(g)] in the raw data, and 294 nm [Fig. S17(h)] after deconvolution.

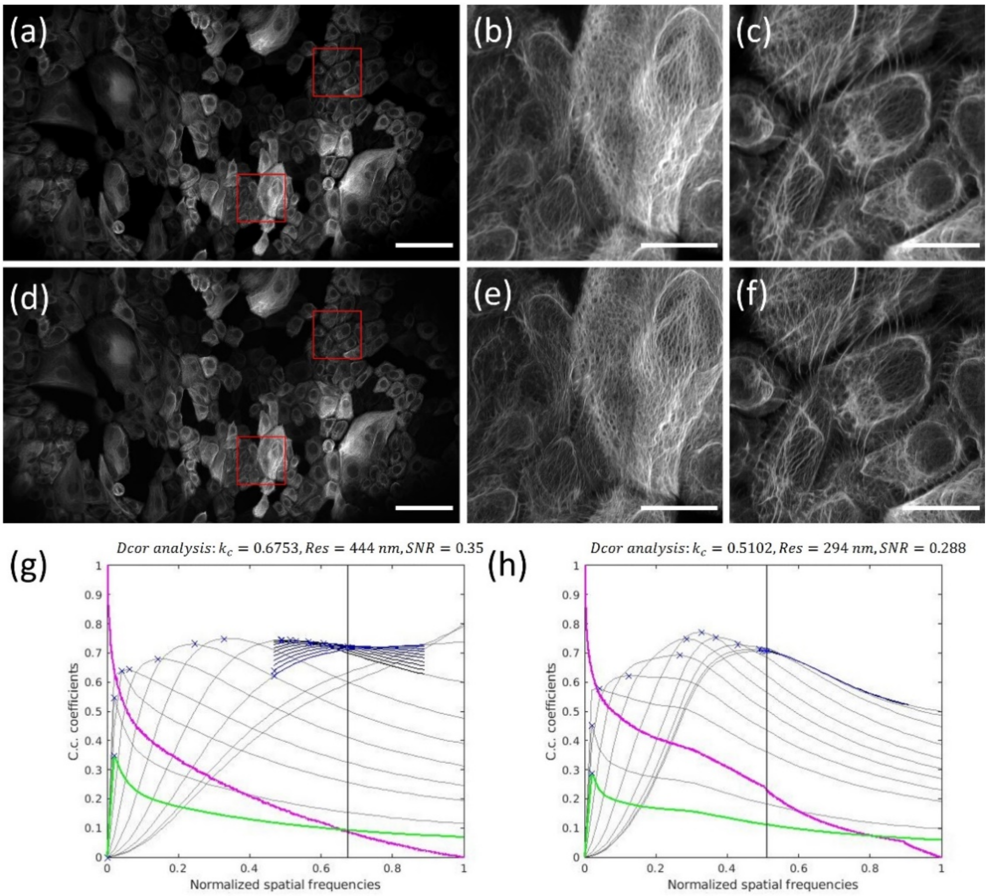

Fig. S17. Maximum projection of human keratinocyte cells expressing mNeonGreen tagged keratin 5. (a-c) Before and (d-f) after up-sampling and deconvolution. (b. c) and (e, f) are the zooms on the red boxed regions in (a) and (d), respectively. (g) and (h) are the decorrelation analysis of (a) and (b), respectively. Scale bars: (a, d) 100 μm, (b, c, e, f) 20 μm.

8. Keratinocyte culture

The hTERT- and Cdk4-immortalized human keratinocyte cell line, Ker-CT (ATCC CRL-4048; gift from J. Shay), [6, 7] was cultured in keratinocyte serum-free medium (K-SFM; 17005042, Thermo Fisher Scientific) on tissue culture dishes coated with bovine type I collagen (PureCol, Advanced BioMatrix).

To create Ker-CT cells stably expressing fluorescently-tagged keratin 5 (K5), a K5-mNeonGreen lentiviral expression construct was created by seamless cloning of K5 (from pBabe-RFP1-KRT5-hygro, Addgene #58493)[8] and mNeonGreen (Allele Biotechnology) fragments into the pLVX-puro vector (Clontech) using HiFi DNA Assembly Master Mix (New England BioLabs) (primers in Table 1). For lentivirus production, this construct was transfected along with packaging constructs psPAX2 and pMD2.G (Addgene #12260 and # 12259) into HEK239 cells (gift from H. Choe) using polyethylenimine (23966, Polysciences). After 48-hours the supernatant was collected, filtered through 0.45-μm mixed cellulose esters membrane syringe filters (09-720-005, Fisher Scientific), and incubated overnight on the target cell line. K5-mNeonGreen-expressing cells were then selected by fluorescence-activated cell sorting on instruments in the Moody Foundation Flow Cytometry Facility.

For imaging, keratinocytes were seeded onto bovine type I collagen-coated glass-bottom plates (D35-20-1.5-N, Cellvis) and grown to 70% confluence. Culture medium was switched to a 1:1 mixture of K-SFM and DMEM/F12 (11320033, Thermo Fisher Scientific) with 2% fetal bovine serum (F0926, Sigma-Aldrich) 24-hours prior to imaging to stimulate cell-cell adhesion and desmosome formation.

Table 1: Primers

K5 fwd	GATCTATTTCCGGTGAATTCCTCGAGGCCACCATGTCTCGCCAGTCAAGTGTG
K5 rvs	GTACAAGAAAGCTGGGTCGCTCTTGAAGCTCTTCCGGGAG
mNG fwd	GACCCAGCTTTCTTGTACGTGAGCAAGGGCGAGGAG
mNG rvs	GAGAGGGGCGGGATCCTTACTTGTACAGCTCGTCCATGCC

9. General guidelines for stitching data

Generally, when one performs tiling, one must specify the degree of overlap between adjacent image tiles. This in large part depends on the specimen. For densely labeled, feature rich specimens, minimal overlap often suffices (e.g., 5%). As the density of the specimen or label decreases, greater overlap becomes increasingly necessary (e.g., 30%). Here, for simplicity, we used 20% overlap throughout and performed stitching with BigStitcher [9], regardless of specimen. To improve the quality of computational fusion, we recommend several steps. Once loaded in BigStitcher, 1) the tiles positions are pre-aligned according to their anticipated location from the metadata. 2) To decrease the likelihood of spurious registrations, pairwise stitching is only performed on adjacent tiles with sufficient overlap (e.g., 10%, if the anticipated overlap is 20%). 3) After pairwise registration, only links (e.g., potential registrations) with an R2 > 0.7 are kept, and 4) the remaining links are subjected to a global optimization step. At this stage, we manually visualize the data, especially regions at the tile interfaces, and export the fused data.

10. Colon cancer cell spheroid culture

The colorectal adenocarcinoma cancer cells (DLD1, colon cancer cell line) in spheroid form were made as follows:

Day 1:

1. Warm 1.5% Difco Noble Agar (in PBS) in microwave until it is completely dissolved.
2. For a 96 well plate, add 50 µL of 1.5% Difco Noble Agar to each well using a 12-channel pipette and a reservoir. (Make sure there are no bubbles)
3. Allow agar to set at room temperature (rt).
4. Bring up cells in media with 10% FBS. Count cells. (Can first try media used to culture cells, changing % FBS can help spheroids form)
5. Plate 5,000 cells/well in 200 µL of media. Incubate at 37º C until spheroids form (3-5 days).

Day 4-7:

Pipette up gently to release spheroid from agar. Transfer media with spheroids to a labeled 15 mL conical tube. Let it sit at rt. until spheroids fall to the bottom of the tube.

Discard media carefully and seed organoids on a layer of matrigel or 1% collagen.

11. Segmentation and meshing of 3D imaging volume

To segment and extract the surface mesh, the raw volumetric image intensity is first min-max normalized to [0-1] and contrast stretched between 2% and 99.8% percentile to enhance image features. Contrast limited adaptive histogram equalization (CLAHE) is applied to locally enhance contrast with a kernel size 1/8th of the original volumetric image shape and a clipping intensity limit of 0.01. The result is normalized by contrast stretching between 2% and 99.8% percentile. Maximum likelihood blind deconvolution was applied for 30 iterations to learn a PSF given an initially synthesized PSF. The learnt PSF was then used to deconvolve the image using Wiener-Hunt deconvolution, balance=1, and Laplacian regularization. The deconvolved image is clipped to [0-1], contrast stretched between 2% and 99.8% percentile and standard normalized. The image is clipped between 0 and 4 standard deviations and min-max scaled to [0-1] to obtain the final postprocessed image intensities for segmentation. From this image we obtain the final binary segmentation volume image by deriving and combining three different segmentations. The first segmentation is obtained from Otsu threshold and captures most of the cellular detail. The second segmentation is optimized to capture a smooth inner core shape of the cell/organoid. It is obtained by significant oversmoothing with a Gaussian filter of the postprocessed image, and thresholding with mean+s.d. with morphological hole filling. The third segmentation is optimized for the detection of thin, high-frequency protrusions. It is obtained by computing the difference of Gaussian (DoG) image which enhances image edges given by postprocessed image – gaussian filter (postprocessed_image, sigma=3), then computing and thresholding the normalized DoG image ((DoG-mean(DoG))/4std(DoG) >= 1). The final binary image is smoothed with a Gaussian filter of sigma=1 and meshed at a contour level of 0.5 using marching cubes. The final mesh is obtained after remeshing the marching cubes mesh to obtain a uniform triangular mesh with approximated centroidal voronoi diagram (ACVD) after collapsing small edges. Fluorescence intensities were then mapped onto the mesh by trilinear interpolation at vertex coordinates. The RdYlBu lookup table was used to assign colors to intensity values using 1% and 99% intensity values as the lower and upper clipping limits. Colored meshes were saved as .obj files and rendered using Meshlab. For the timelapse movie, volumetric images were rigid registered temporally using frame 0 as the common reference image and intensities corrected for bleaching with histogram matching to the frame 0. The segmentation described above was applied to obtain meshes for each timepoint.

12. Water reservoir for long-term imaging

The used primary objective has a 2 mm working distance. Due to the inverted geometry of our setup, this requires a long water meniscus, which is prone to evaporation when performing long-term imaging. We used a water reservoir below the coverslip to minimize water evaporation and provide a larger water basin, as shown in Fig. S18.

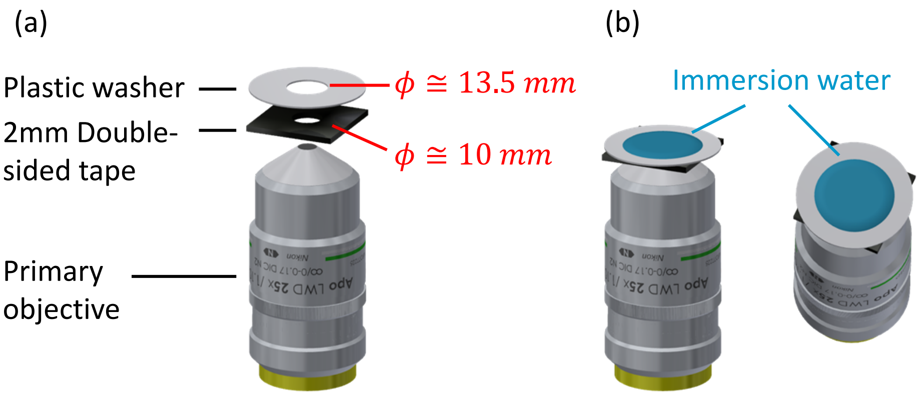

Fig. S18. Water reservoir for long-term imaging. (a) The water reservoir is assembled by adhering a 2 mm thick double-sided tape (Amazon) and a plastic washer (Chemical-Resistant PTFE Plastic Washer, 94115K005, McMaster-Carr) on the primary objective. The double-sided tape is cut to a ~30 mm square with a ~ 10 mm hole. The plastic washer has an inner diameter of 0.532 inches. (b) A large amount of immersion water (compared to a conventional water meniscus) can be added. Although it still slowly vaporizes, water levels stay sufficiently high for imaging for at least 24 hours.

13. Natural killer cell culture

The NK-cells were labeled in the following way:

1. Resuspend CellTracker Red CMPTX to a 1 mM solution in DMSO and warm in a 37°C water bath.
2. Wash human NK cells twice with warm PBS and resuspend cells in serum-free media with a 1:1000 dilution of CellTracker Red CMPTX. Incubate at 37°C for 1-2 hours.
3. Wash NK cells with warm serum-free media 3x for 20 minutes each at 37°C.
4. Replace with desired media.

Once stained, human NK cells were cocultured with MCF7 cancer cells (estrogen and progesterone receptor positive cell line) that were transduced with GFP. Imaging took place 4-6 hours after coculture began.

References

1. Heintzmann, R., *A Appendix: Practical Guide to Optical Alignment*, in *Fluorescence Microscopy*. 2013. p. 393-401.
2. Huisken, J. and D.Y.R. Stainier, *Even fluorescence excitation by multidirectional selective plane illumination microscopy (mSPIM)*. Optics Letters, 2007. **32**(17): p. 2608-2610.
3. Venkateswaran, N., et al., *MYC promotes tryptophan uptake and metabolism by the kynurenine pathway in colon cancer.* Genes & Development, 2019.
4. Chang, B.-J., et al., *Real-time multi-angle projection imaging of biological dynamics.* Nature Methods, 2021. **18**(7): p. 829-834.
5. Descloux, A., K.S. Grußmayer, and A. Radenovic, *Parameter-free image resolution estimation based on decorrelation analysis.* Nature Methods, 2019. **16**(9): p. 918-924.
6. Vaughan, M.B., et al., *H-ras expression in immortalized keratinocytes produces an invasive epithelium in cultured skin equivalents.* PLoS One, 2009. **4**(11): p. e7908.
7. Ramirez, R.D., et al., *Bypass of telomere-dependent replicative senescence (M1) upon overexpression of Cdk4 in normal human epithelial cells.* Oncogene, 2003. **22**(3): p. 433-44.
8. Wang, C.C., et al., *A time- and matrix-dependent TGFBR3-JUND-KRT5 regulatory circuit in single breast epithelial cells and basal-like premalignancies.* Nat Cell Biol, 2014. **16**(4): p. 345-56.
9. Hörl, D., et al., *BigStitcher: reconstructing high-resolution image datasets of cleared and expanded samples.* Nature Methods, 2019. **16**(9): p. 870-874.